14 Mar 1991, 10:30 am - 12:30 pm

Liquefaction Analysis by Multi-Surface Model

Satoshi Morio

Technical Research Institute, OKUMURA Corporation, Japan

Proceedings: Second International Conference on Recent Advances in Geotechnical Earthquake Engineering and Soil Dynamics, March 11-15, 1991, St. Louis, Missouri, Paper No. 3.45

Liquefaction Analysis by Multi-Surface Model

Satoshi Morio
Senior Research Engineer, Technical Research Institute,
OKUMURA Corporation

SYNOPSIS: In recent years, liquefaction phenomena induced by earthquakes have attracted considerable attention and extensive research has already been performed on various aspects. Also, many constitutive relations have been proposed in order to represent the deformation behavior during cyclic loading. These models, however, have mostly been verified by comparison stress or strain control element tests, and there have not been many numerical tests applying them to the boundary value problems.

In this study, a simple and practical constitutive relation which is able to simulate the unelastic behavior of soils under multi-directional cyclic stresses is proposed. The proposed model has been introduced with the computer code (DIANA-J), and the accuracy of this model is examined by comparing the numerical results with the experimental ones.

1. INTRODUCTION

Since deformational behaviour of soils during cyclic loading is known to depend greatly upon the initial stress state and the stress path, constitutive equations accurate enough to express those characteristics are needed.
The major constitutive equations of soils so far proposed have been based on elastoplastic theory and most of them on the isotropic hardening rule. To suitably express hysteresis behaviour such as the accumulation of volumetric strain and the Baushinger effect during cyclic loading, however the anisotropic hardening rule needs to be adopted.

There have been cyclic models employing the anisotropic hardening rule such as the bounding surface model(Mroz,1979) and the model based on the concept of the field of hardening moduli (Mroz,1975). But few attempts have been made to introduce those models in the finite element method program and to apply them to various boundary value problems.

This paper proposes an anisotropic hardening model representing the behaviour of sand during cyclic loading for the purpose of two-dimensional liquefaction analysis.
For easy handling, the model has been simplified as much as possible with the fewest possible parameters.

After introducing this model in the two-phase finite element program (DIANA-J; Shiomi,1984) based on the effective stress, the analysis of element tests (undrained simple shear tests), the analysis of the ground liquefaction at Kawagishi-cho during the Niigata Earthquake (one-dimensional problem) and the simulation analysis of the centrifuge test (two-dimensional problem) are presented.

They are all on the agenda of the research committee on the behaviour of ground and soil constructions during earthquake(Ishihara et al., 1989) in the Japanese Society of Soil Mechanics and Foundation Engineering.

This paper represents the details of the above analyses, and the applicability of this model to liquefaction analysis is investigated.

2. ANALYSIS METHOD

(1) Outline of the Multi-Surface Hardening Model

The concept of the field of hardening moduli is used in this research. The field of hardening moduli(Mroz,1975) is determined according to the arrangement of an infinite number of surfaces having a certain hardening modulus in the stress space. This model is composed of three types of surfaces ; the bounding surface F, the loading surface f and stress reversal surface f_s.

The bounding surface F plays the role of the failure surface. The loading surface f is defined inside F (by interpolation) as an infinite number of surfaces of the similar figure. The plastic behaviour of material is given by the translation and the expansion (contraction) of f.

Figure 1 is an illustration of the outline of this model on a two-dimensional stress plane. The horizontal axis is for the deviatoric stress ratio, the vertical axis for the shear stress ratio. σ_a' is the effective axial stress, σ_r' the effective lateral stress, τ_d the shear stress and σ_m' the effective mean stress.

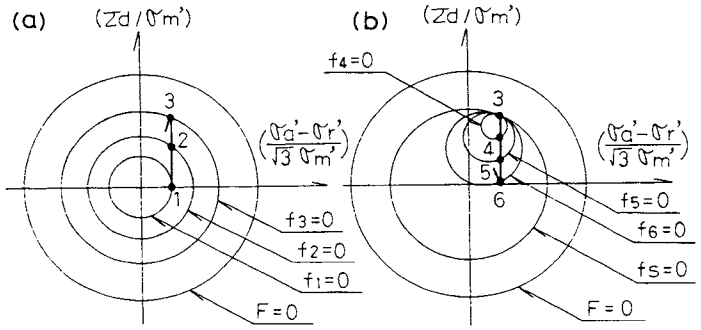

Figure 1 Outline of this model

(a) in the figure denotes the loading surface f and the bounding surface F in the shear process from the point 1 to the point 3 in the anisotropic stress state. At the point 1, $\tau_d = 0$, and $\sigma_a' > \sigma_r'$, with the loading surface represented by f_1. As τ_d increases, the loading surface expands, reaching f_3 at the point 3. (b) in the figure denotes the reversed shear process from the point 3 to the point 6. As soon as the load is reversed, the loading surface appears as a dot on f_3.

The loading surface immediately before load reversal is defined as a stress reversal surface fs. After the load reversal, f increases as the reversed shear progresses. This suggests that in the process from the point 1 to the point 3 f_1 and f_2, both situated inside the point 3, have been translated by the stress point.

As understood from the above, all the translation of the stress ratio in the deviatoric stress ratio space is assumed to be a load (hardening) in this model, and caused the plastic deformation to occur.

When the stress point is on f with stress increment vector outside f, the hardening moduli, i.e., the plastic strain increment, is obtained by using the interpolation function in the later described equation 14) on the basis of the magnitude (radius) of f. On the other hand, when the stress point is on F with stress increment vector outside F, the plastic strain increment is obtained in such a way as to fulfill the consistency condition.

(2) Fundamental Equations of the Model

The bounding surface F is given by the equation 1), which coincides with the Drucker-Prager model if the cohesion C = 0.

$$F = (1/2)\,\eta_{ij}\eta_{ij} - A^2 \quad \text{---------- 1)}$$

Where $\eta_{ij} = S_{ij}/\sigma_m'$, S_{ij} being the deviatoric stress, A is the radius of F and $A = 2\sqrt{3}\sin\phi / (3 - \sin\phi)$, ϕ being the internal friction angle at the failure.

In this model, the hardening of F is not considered, and the loading surface f is always established so as to have the present stress point on it, given by the equation 2).

$$f = (1/2)\,(\eta_{ij} - \alpha_{ij})(\eta_{ij} - \alpha_{ij}) - A_o^2 \quad \text{--2)}$$

Where α_{ij} is the coordinates of the centre of f and A_o the radius of f. In the case of material having the cohesion C, the same treatment is possible by using $\sigma_m' - C\cdot\cot\phi$ instead of σ_m in the equations 1) and 2).

The plastic strain increment $d\varepsilon_{ij}^P$ is given by the equation 3) where the unit normal vector n_{ij} for the loading surface, the unit vector g_{ij} defining the direction of the plastic strain increment, the effective stress increment $d\sigma_{ij}$ and the hardening modulus K_P are used.

$$d\varepsilon_{ij} = (1/K_P)(n_{ij}\,d\sigma_{ij})\,g_{ij} \quad \text{---------- 3)}$$

n_{ij} and g_{ij} are given by the equations 4) and 5) respectively. For Q in the equation 5), the Cam-Clay type's plastic potential surface is used which is defined in the equation 6). The load reversal is judged from the reversing of the sign of $d\sigma_n$ in the equation 7).

$$n_{ij} = \frac{\partial f/\partial \sigma_{ij}}{\{(\partial f/\partial \sigma_{ij})(\partial f/\partial \sigma_{ij})\}^{1/2}} \quad \text{---- 4)}$$

$$g_{ij} = \frac{\partial Q/\partial \sigma_{ij}}{\{(\partial Q/\partial \sigma_{ij})(\partial Q/\partial \sigma_{ij})\}^{1/2}} \quad \text{---- 5)}$$

$$Q = A_o / M_m + \ln \sigma_m' \quad \text{---------- 6)}$$

$$d\sigma_n = n_{ij}\,d\sigma_{ij} \quad \text{---------- 7)}$$

Mm is given by $Mm = 2\sqrt{3}\sin\phi_m / (3 - \sin\phi_m)$, where the internal friction angle ϕ_m at the maximum volume contraction is used. $d\sigma_{ij}$ is given by the equation 8) or, if the total strain increment $d\varepsilon_{ij} (= d\varepsilon_{ij}^E + d\varepsilon_{ij}^P)$ is known, by the equation 9).

$$d\sigma_{ij} = D^E\,d\varepsilon_{ij} \quad \text{---------- 8)}$$

$$d\sigma_{ij} = D^{EP}\,d\varepsilon_{ij} \quad \text{---------- 9)}$$

$$D^{EP} = D^E - \frac{n_{ij}\,D^E \cdot D^E\,g_{ij}}{K_P + n_{ij}\,D^E\,g_{ij}}$$

Here $d\varepsilon_{ij}^E$ is the elastic strain increment, and D^E the elasticity matrix. The shear modulus G and the bulk modulus K, both composing D^E, are given by the following equations.

$$G = G_o(\sigma_m'/\sigma_{mo}')^{1/2} \quad \text{---------- 10)}$$

$$K = K_o(\sigma_m'/\sigma_{mo}')^{1/2} \quad \text{---------- 11)}$$

Where σ_{mo}', G_o and K_o are the initial effective mean stress, and the initial value of G and that of K respectively.

In the case of $f \neq F$, a new loading surface f^K is formed every time the stress point is translated in the deviatoric stress ratio (η_{ij}) space. Then, the coordinates α_{ij}^K of the centre of f^K and its radius A_o^K are determined in such a way as to satisfy the equation 2) and the following equation 12).

$$\alpha_{ij}^K = \frac{\alpha_{ij}^I(A_o^S - A_o^K) + \alpha_{ij}^S(A_o^K - A_o^I)}{A_o^S - A_o^I} \quad \text{--12)}$$

Where the suffixes K, I and S are the index of quantities of the active loading surface, previous loading surface and the bounding surface or

stress reversal surface respectively. This principle is established so that any surface can not be intersected with each other, and is the same as the rule in the deviatoric stress (S_{ij}) space of the INS model (Morio, 1989) formulated in the three-dimensional stress space.

Figure 2 illustrates the equation 12) on the same plane as Figure 1. In Figure 2, the active loading surface is denoted by f^K and the previous surface by f^I.

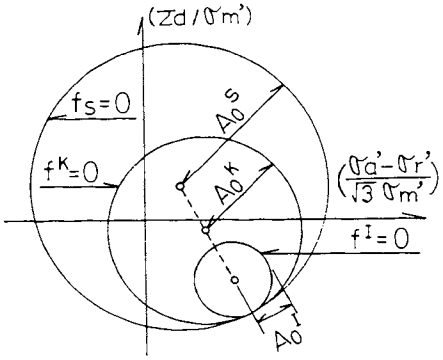

Figure 2 Hardening rule

The equation 12) expresses the fact that the centre of f^K is determined on the line established by joining the centre of f^I and that of f^S. In other words, using the radius expansion dA_0 ($= A_0^K - A_0^I$), the translation $d\alpha_{ij}$ ($=\alpha_{ij}^K-\alpha_{ij}^I$) of the centre of the loading surface is expessed by;

$$d\alpha_{ij} = (\alpha_{ij}^S - \alpha_{ij}^I)\, dA_0 / (A_0^S - A_0^I) \quad --13)$$

When the hardening rule in the equation 12) and the later described equation 14) are used, this model satisfies the Masing rule in the case where σ_m' is constant.

As far as this kind of multi-surface model is concerned, many stress reversal surfaces should be memorized in the case of the cyclic loading with decreasing amplitudes. This makes the model more complicated (Hashiguchi, 1985; Norris, 1986). To cope with this problem, only the latest stress reversal surface is memorized in this model as in Mroz's INS model (Mroz, 1981). And then, a new stress reversal surface is defined, as shown in Figure 3, in the case where the stress point goes beyond this latest stress reversal surface. In the figure, the stress reversal surfaces at points A, B and C, when stress reversal occurs in this order, and are denoted by f_{SA}, f_{SB} and f_{SC} respectively. However, if every stress reversal surface is expressed actually, A_0^K and α_{ij}^K are determined, f_S being f_{SC}, when the stress point is inside f_{SC}, being f_{SB} when the point is inside f_{SB} and outside f_{SC} and being f_{SA} when the point is inside f_{SA} and outside f_{SB}. That is to say, an infinite number of f_S need to bememorized, so the memory area for the program and the CPU time need to be increased.

In this model, when the stress point is inside f_{SC}, only the latest stress reversal surface f_{SC} is memorized. Afterwards, when the stress point goes beyond f_{SC}, a new stress reversal surface f_{SD} on the periphery of f_{SC} is defined by the centre the origin. The use of this f_{SD} allows the smooth interpolation of A_0 and the hardening modulus K_P and at the same time economizes the memory area for the program.

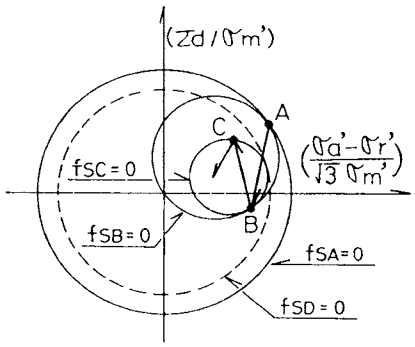

Figure 3 New stress reversal surface

The interpolation rule for K_P is as follows.

$$K_P = K_{PO} (\sigma_m' / \sigma_{mo}')^n (1 - A_0/A)^m \quad --14)$$

Where $K_{PO} = a \cdot G_o$ with a, n and m the parameters of this model. The above equation is analogous to Ghaboussi's hardening modulus interpolation rule (Ghaboussi, 1984). But in our research, n = 1 and m = 2 are used. In the case of n = 1 and m = 2, the $A_0 - \varepsilon_s^P$ (ε_s^P:the second-order invariable of plastic deviatoric strain) relation during the virgin loading (skeleton curve) is expressed as hyperbolic. Then, K_{PO} is determined by the initial tangential slope of the hyperbola, and A is the asymptote.

(3) Solution Method of Nonlinear Equations

The analysis in 3. (1) below does not use DIANA-J, so convergence calculation is not performed. Since it is the analysis of undrained simple shear tests, the equation 9) is used to control the shear stress by specifing both the lateral strain increment and the vertical strain increment as zero and the shear strain increment as (1×10^{-5}).

In 3. (2) and (3) the initial stress method is adopted for convergence calculation. However, in the two-phase dynamic analysis a small load reduction (stress reversal) occurred in the convergence process (though none in the static analysis). Since this load reduction can not be assumed in this model to be the stress hysteresis, the stress increment was calculated by using a strain increment from the strain at the start of each convergence process.

3. ANALYSIS RESULTS

(1) Analysis of Element Tests (Undrained Simple Shear Tests)

The analysis of the element tests for 8m to 14 m ground level at Kawagishi-cho (later described figure 6) was conducted using the material constants ($\phi = 37°$, $\phi_m = 27°$, G_o = 65030 KPa

and Poisson's ratio $\nu = 0.2$) .

The parameter a was determined, as specified by the committee, so that the resistance against liquefaction will agree with the experimental results. As a result, a = 12 was used.

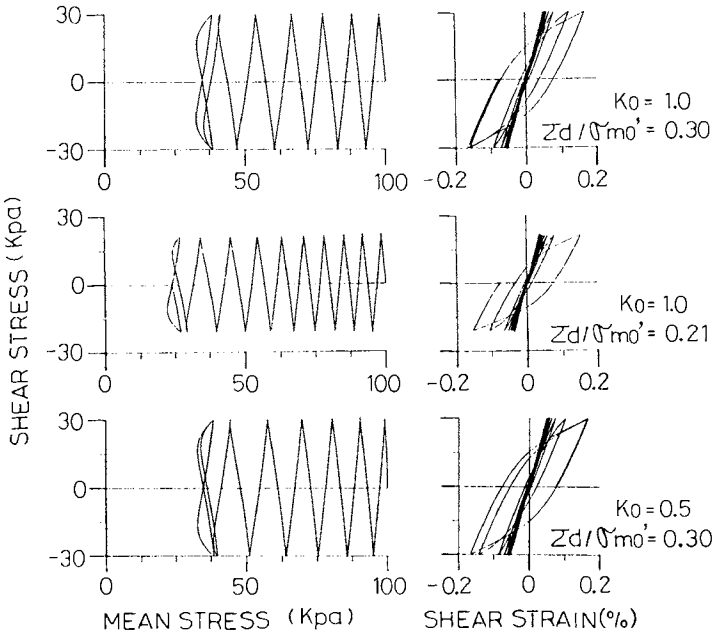

Figure 4 Simulation analysis of element tests

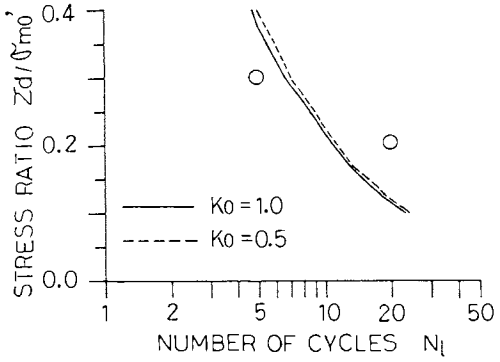

Figure 5 Liquefaction resistance curve

Figure 4 illustrates the effective stress path and the stress-strain relation when the stress ratio is $\tau_d/\sigma_{mo}' = 0.3$, 0.21 with the isotropic consolidation $K_o = 1.0$ ($\sigma_{xo}' = \sigma_{yo}' = \sigma_{zo}' = 98$ kPa) and when $\tau_d/\sigma_{mo}' = 0.3$, with anisotropic consolidation $K_o = 0.5$ ($\sigma_{xo}' = \sigma_{zo}' = 73.5$ kPa, $\sigma_{yo} = 147$ kPa) .
Note that σ_{xo}' and σ_{zo}' are the initial effective lateral stresses and σ_{yo}' is the initial effective vertical stress.

In Figure 4, as the behaviour of the cyclic mobility is shown, there is an increasing strain. But, the strain is as small as 0.17%. Only 1 to 2 cycles after the start of the cyclic mobility, the effective stress path and the stress-strain relation become a steady state. Therefore, the number of cycles at the beginning of the steady state is assumed as the resistance against liquefaction.

The liquefaction resistance curve is shown in Figure 5. The experimental results are marked with ○ in the figure. Since the slope of the liquefaction resistance curve is steep in the case of this model, it has been impossible to correctly express the experimental results.

Therefore, parameter a has been established in Figure 5 so that the centre between the given two points will be passed.

The following will be understood from Figures 4 and 5.

① When the resistance against liquefaction is expressed by using τ_d/σ_{mo}', this model has almost the same liquefaction resistance between $K_o = 0.5$ and $K_o = 1.0$.

② This model can not express the soil behaviour while strain begins to increase after the phase transformation line and grows into a large strain. A solution to this matter may be to decrease K_{PO} in the equation 14) under an undrained condition by assuming it to be a function for plastic shear strain or the accumulation of shear work. But it is not yet certain whether this method can be applied to a case where effective stress recovers under drained condition.

③ The pore pressure occurring during the first cycle is smaller than that of later cycles.

(2) One-Dimensional Analysis of the Ground at Kawagishi-cho during the Niigata Earthquake

a. Analysis Conditions

The ground at Kawagishi-cho during the Niigata Earthquake (with depth 70m and groundwater level 2m) was divided into 20 elements shown in Figure 6. Then, the analysis was conducted by entering a seismic wave with maximum 120 cm/s² (twice as large as the incident wave) from the lower end of the viscous dashpot attached to the base of the soil model.

The input accelerogram is shown in Figure 7. This wave is the result of modifying the strong earthquake wave recorded at the basement of the Akita Prefectural Office with respect to the difference in epicentre distance and distance attenuation (Ishihara et al.,1989).

The initial stress state K_o is 0.5.
And an undrained condition is assumed. For time integration Newmark's β scheme is adopted.
The size of the time increment is 0.005 sec, and the coefficients of the Rayleigh damping is $\alpha = 0.0$ and $\beta = 0.001$. The parameter a of this model is shown in Figure 6. The curves for the resistance against liquefaction worked out from these constants are shown in Figure 8.
The experimental results for each depth are also shown in the figure.

The linear elastic model is used for the ground level 0m to 2m, and the Drucker-Prager model for the level 14m to 70m.

b. Results of the Analysis

Figure 9, 10 and 11 are the time history of

Depth (m)	Element Number	Vs (m/s)	Density (t/m³)	Relative Density (%)	G_o (KPa)	σ_v' (KPa)	ϕ (Degree)	τ_{xy}/σ_{mo}'		a
								R_5	R_{20}	
1	1	110	1.8		21780	8.82	30			
2	2					26.46				
3.5	3	110	1.9	30～40	22990	41.90	31	0.10	0.09	5
5	4					55.13				
6.5	5	150	1.9	45	42750	68.36	35	0.15	0.11	8
8	6					81.59				
10	7	185	1.9	50～55	65030	97.02	37	0.20	0.14	12
12	8					114.70				
14	9					132.30				
17	10	230	2.1	80～85	111100	157.30	44	0.70	0.50	
20	11					189.60				
24	12					227.40				
28	13					270.50				
34	14	270	2.2	90	160400	327.30	45	0.90	0.60	
40	15					397.90				
46	16					468.40				
52	17					539.00				
58	18					609.60				
64	19					680.10				
70	20					750.70				
		350	2.3	ϕ_m = 28 ° (GL-2～14 m)、Poisson's Ratio ν = 0.2 (All Element)						

Figure 6 Model of the ground at Kawagishi-cho

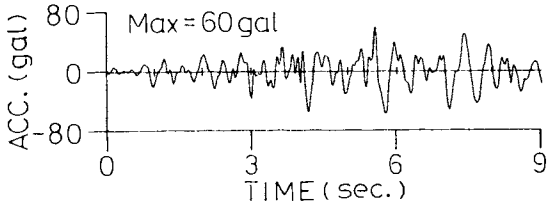

Figure 7 Input accelerogram

acceleration, shear stress and pore pressure. Referring to Figure 11, the pore pressure becomes equal to the initial vertical effective stress in about 4 seconds at ground level 3.5 to 5m and in about 6 seconds at ground level 2 to 3.5m, resulting in liquefaction. This result may not seem very different from that of the other seven models (Isihara et al.,1989). But closer examination will reveal that the increase of pore pressure at ground levels 2 to 3.5m and 10 to 12m is a little larger in this model. It is probably because the slope of the liquefaction resistance curve, as illustrated in Figures 5 and 8, is steeper in this model, with the result that the pore pressure increase at low stress ratio has been overestimated. Figures 9 and 10 show that the shear stress amplitude and the acceleration amplitude become smaller at the ground levels above 3.5m after the liquefaction occurs in about 4 seconds at the level 3.5 to 5m. This is a typical response observed in the liquefied ground and the shaking table experiment, etc.

Figure 12 illustrates the distribution of

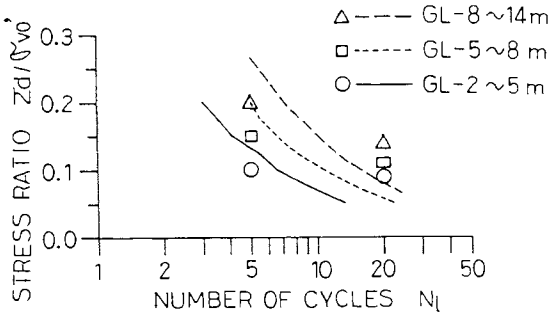

Figure 8 Liquefaction resistance curve

maximum acceleration and maximum displacement by depth. The distribution may not seem very different from that of other models in form and the absolute value. But if closely studied, the values around ground level 5 to 12m seem larger. Yet, direct comparison between the models is impossible here, because damping and convergence criteria are not specified.
The maximum acceleration in about 6 seconds is shown by an arrow in Figure 9.

Figures 13,14 and 15 illustrate the time history of the effctive stress (σ_x', σ_y', σ_m') , the effective stress path and the stress-strain relation at ground levels 3.5 to 5m and 6.5 to 8m. In Figures 14 and 15, the tendency is expressed for the secant modulus for the relation between stress and strain to decrease but for the hysteresis damping to increase.

Especially at ground level 3.5 to 5m, permanent strain is accumulated, causing a large

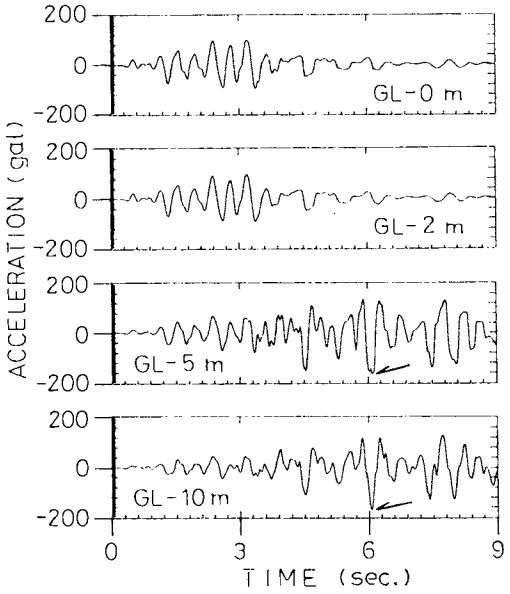

Figure 9 Time history of acceleration

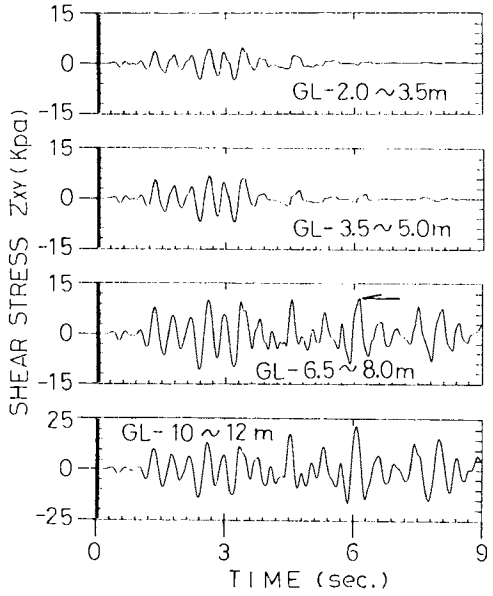

Figure 10 Time history of shear stress

strain of about 1.4%. Moreover, when cyclic mobility occurs, the relation between stress and strain shows little reversal.

In Figure 13, in which the process is well expressed, K_o = 0.5 rises into K_o = 1.0 only after the vertical effective stress σ_y' greatly decresses at an early stage when the lateral effective stress σ_x' shows little decrease.

In Figures 10, 14 and 15, the peak shear stress corresponding to the maximum acceleration in about 6 seconds is marked with an arrow for the ground level 6.5 to 8m. The reason for the increase of acceleration in the range of the ground level 5 to 12m is thought to be the occurrence of a large shear stress due to the recovery of the effective stress on the phase transformation line.

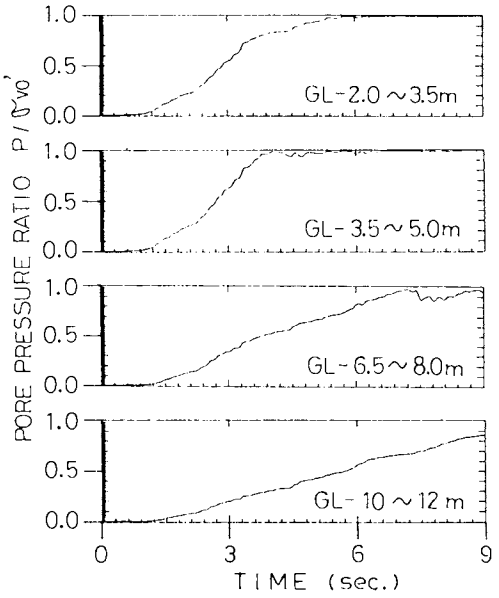

Figure 11 Time history of pore pressure

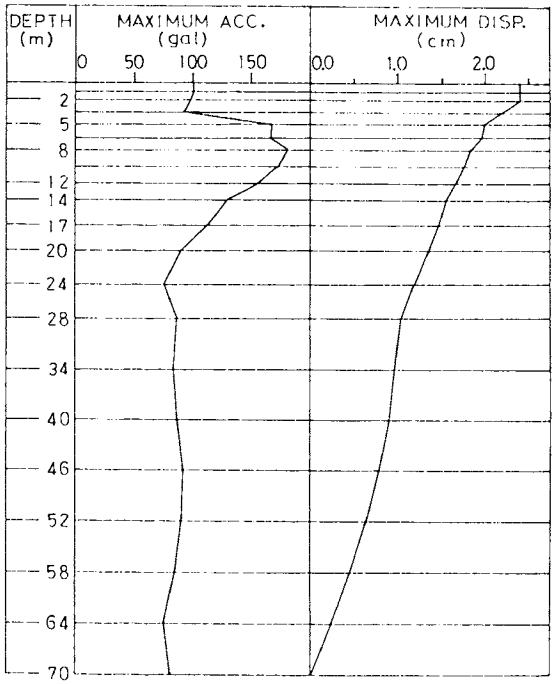

Figure 12 Maximum response

(3) Simulation Analysis of Centrifuge Test

a. Analysis Conditions

The subject is an oscillation test for a submerged (in silicon oil) embankment on the Cambridge Geotechnical Centrifuge. The test was carried out at a centrifuge gravity level of 41.8g. The input seismic wave is a pseudo sine wave at 58.8Hz, and the maximum acceleration 20 %G (representing a percentage of 41.8g). The wave, by means of a 200Hz low-pass filter, was used in the analysis, as shown in Figure 16. The divided elements used for the analysis is shown in Figure 17. The figure is provided

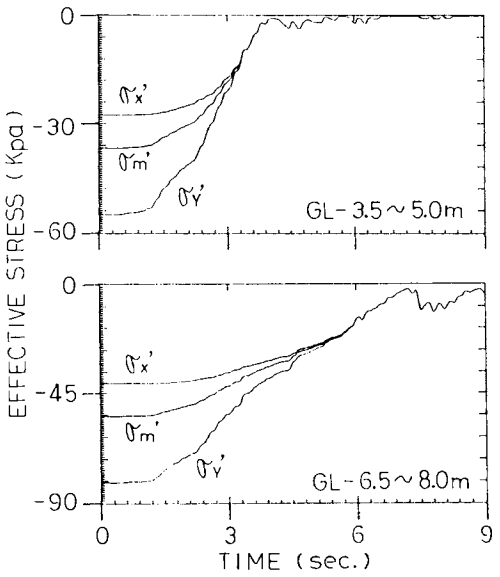

Figure 13 Time history of effective stress

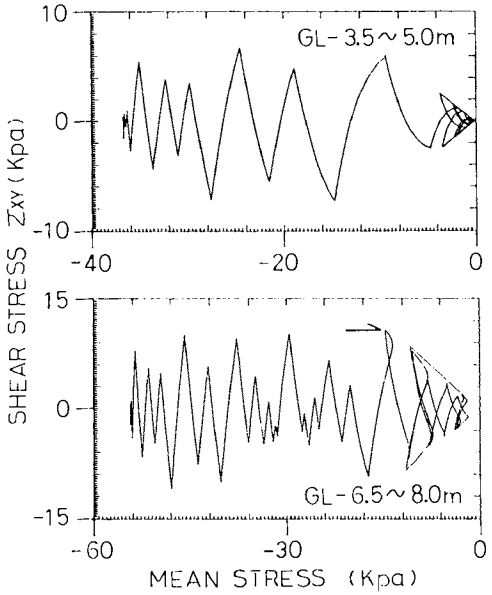

Figure 14 Effective stress path

with node numbers (NP) and element numbers (enclosed in squares) for comparison between the results of the test and those of the analysis.

The model is submerged fully. And an undrained condition is assumed.

The initial stress has been decided as follows. First, the linear elastic gravity analysis was conducted at the level of 41.8g and then the initial shear modulus G_o from the resultant σ_m' of each element was obtained by using $G_o = 8672\ (\sigma_m')^{1/2}$ kPa. Once more the linear elastic gravity analysis was conducted, using this G_o and the Poisson's ratio $\nu = 0.3$, and the resultant stress was assumed to be the initial stress. But note that for elements whose ratio K_o between lateral effective stress and vertical effective stress is less than 0.4,

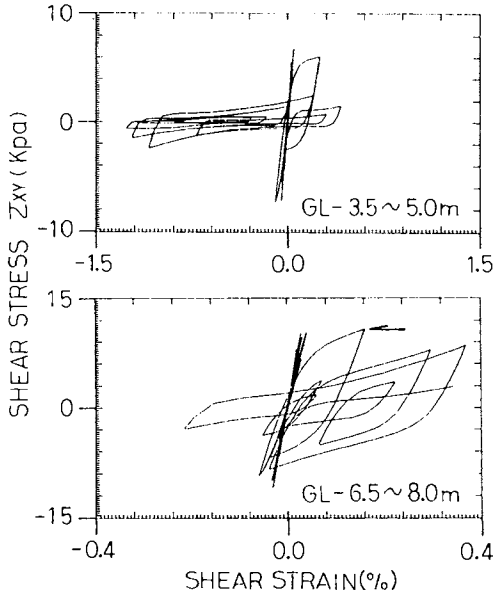

Figure 15 Shear stress and shear strain

Table 1 Material properties of sand

True Specific Gravity	Gs	2.65
Relative Density	Dr	60 %
Initial Void Ratio	e_o	0.8
Initial Shear Modulus (at $\sigma_m' = 98$ KPa)	G_o	85838 KPa
Poisson's Ratio	ν	0.3
Angle of Shear Resistance	ϕ	39°
Angle of Phase Transformation Line	ϕ_m	32°
Resistance against Liquefaction τ_{xy}/σ_{mo}' (Cyclic Number N=20)	R_{20}	0.13

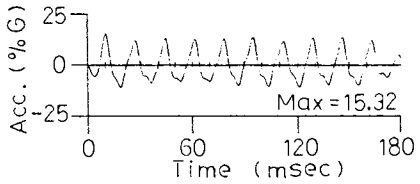

Figure 16 Input accelerogram

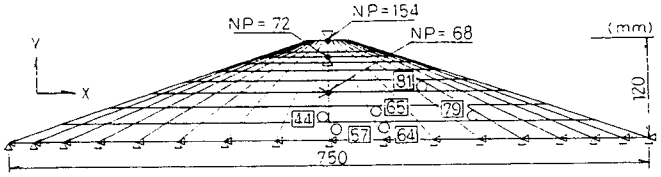

Figure 17 Model for the analysis

the lateral effective stress was modified to make sure that $K_o = 0.4$.

The same specification as in 3. (2) has been given to time integration and the coefficient of the Rayleigh damping, but the size of the time increment has been specified as 0.1 msec.

The material properties used for the test are shown in Table 1. The parameter of this model has been specified as a = 25. The curve for the liquefaction resistance in the vicinity of the

centre of the embankment is established by using the average σ_m', as shown with a solid line in Figure 18. The circle in the figure denotes the resistance against liquefaction designated by the committee. Because only one point was designated, we have considered the resistance curve like the coloured one and specified the parameter so that the centre will be passed as in Figures 5 and 8 .

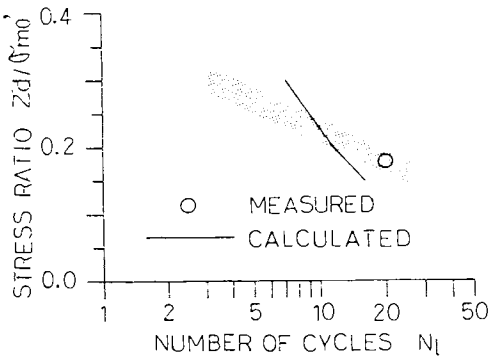

Figure 18 Liquefaction resistance curve

b. Results of the Analysis

Figures 19 and 20 show the comparison between the analysis result and the test result for the time history of pore pressure and acceleration time history respectively. Concerning the time history of pore pressure, good agreement is achieved between both results.

But pore pressure increases with large fluctuations during the test, while with only small fluctuations in the analysis. That is probably because of the effect of the dynamic pressure of liquid (silicon oil) during the test. Generally speaking, fluctuation in pore pressure depends on the change of total stress or on cyclic mobility. The small fluctuations in the analysis are thought to be caused by the former, for their period is the same as that of the input wave.

On the other hand, concerning acceleration time history the analysis result does not agree with the test result very well. The decrease of acceleration amplitude in response to the rise in pore pressure during the test contrasts with the almost fixed amplitude of acceleration in the analysis. Though no definite cause has been found, there is a possibility of the input of the initial stress σ_{mo}' being too large in the analysis.

Figure 21 illustrates the deformation pattern and the contour diagram of the pore pressure distribution at the end of the earthquake (in 0.18 seconds). Above the line with pore water pressure zero, there is small negative pore pressure of approximately 0 to -3 kPa. The final settlement of the top of the embankment is reported to be about 2 mm during the test. But the analysis result shows a small settlement, about 0.1 mm.

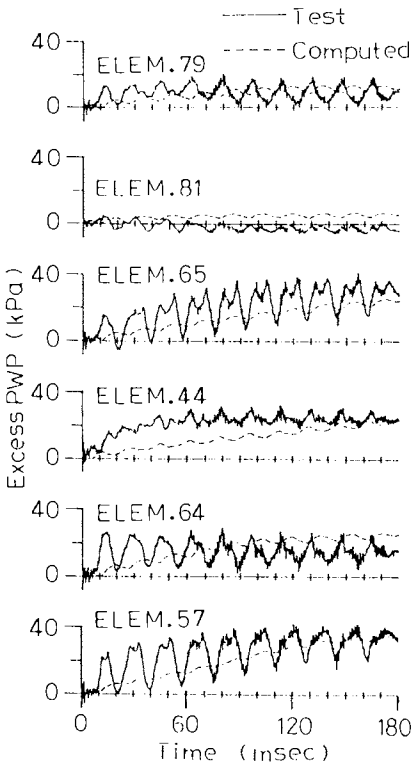

Figure 19 Time history of pore pressure

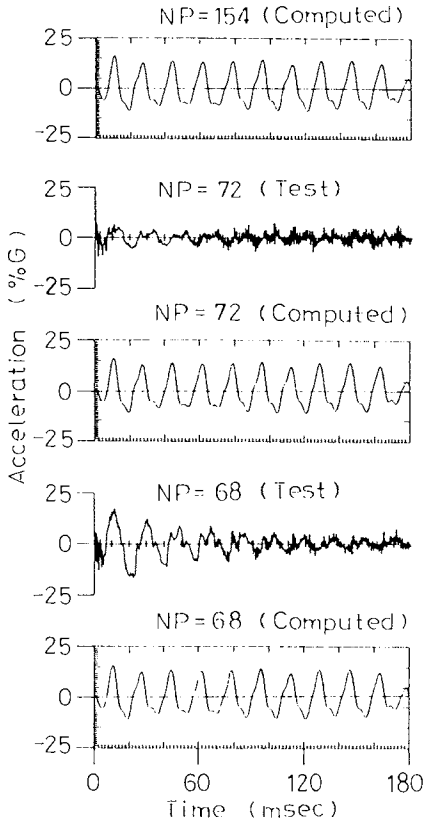

Figure 20 Time history of acceleration

Figure 22 shows the relation between shear stress and shear strain and the effective stress path for both elements 44 and 57. Element 44 is

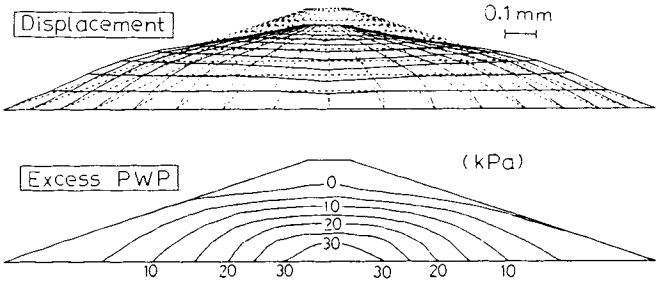

Figure 21 Deformation pattern and pore pressure distribution contour diagram

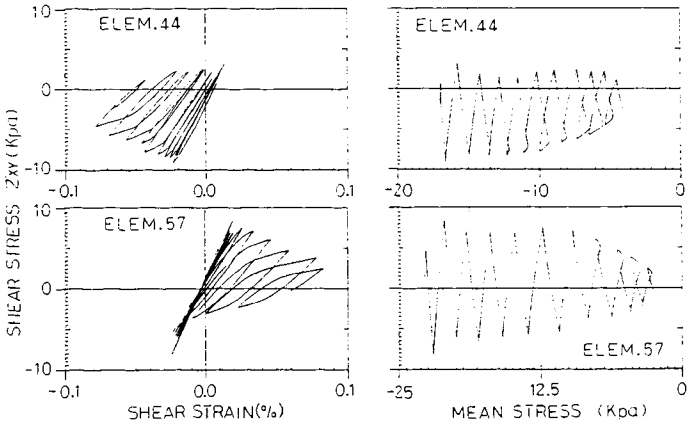

·Figure 22 Stress path and stress-strain relation

positioned on the left side of the embankment, having negative initial shear stress. Element 57 is on the right side of the embankment, having positive initial shear stress. Figure 22 illustrates the tendency for shear strain to accumulate in the direction of this initial shear stress. It is because the hardening modulus K_P becomes smaller (i.e., the radius A_0 of the loading surface expands) as the shear stress works in the direction of the initial shear stress. In addition, the figure shows the tendency for the shear stress amplitude to decrease after the sixth wave (in about 100msec) in response to the rise in pore pressure.

The deformation pattern shown in Figure 21 represents the sum of the deformation due to the (permanent) shear strain depicted in Figure 22 and another one resulting from the gravity under the condition of the decrease in soil strength in response to the rise in pore pressure.

This analysis has been carried out under an undrained condition. Considering the dissipation of pore pressure after an earthquake, it is expected that some different results will be drawn.

4. CONCLUSION

An anisotropic hardening rule which does not allow the intersection of the bounding surface, the loading surface and the stress reversal surface in the deviatoric stress ratio (η_{ij}) space is proposed.

Also, the definition of a new stress reversal surface allows the smooth interpolation of the hardening modulus K_P and at the same time economizes the memory area for the program.

This multi-surface model uses these five parameters : the initial shear modulus G_0, the initial bulk modulus K_0, the internal friction angle Φ at the failure, the internal friction angle Φ_m at the maximum volume contraction and a used for the equation 14). The parameter a has been determined according to the simulation of element tests so that the liquefaction resistance curve will agree with the given condition.

After introducing this model in a two-phase finite element program based on the effective stress, one and two-dimensional liquefaction analysis was conducted. The analysis results are not very different from those for the other seven models (Ishihara et al., 1989). In view of the necessity of improvements such as by the research on intensity anisotropy, this model will be a useful tool for liquefaction analysis.

Incidentally, CPU time spent on the two-dimensional analysis in 3. (3) is 75 minutes on IBM-4381 (3.8 MIPS).

REFERENCES

Ghaboussi,J.(1984), "Plasticity model for inherently anisotropic behaviour of sands", Int. Jour.for Num.and Anal.Meth.in Geo., Vol.8

Hashiguchi,K.(1985), "Two-and three-surface models of plasticity", 5th Int.Conf.on Num. Meth.in Geo. (Nagoya)

Ishihara,K. et al.(1989), "Symposium on the behaviour of ground and soil constructions", Japanese Society of Soil Mechanics and Foundation Engineering (in Japanese)

Morio,S., Kusakabe,S. & Hyodo,M.(1989), "The applicability of INS Model to the liquefaction analysis", Journal of Structural Engineering", Vol.35A (in Japanese)

Mroz,Z.(1975), "On the description of anisotropic workhardening", Journal of the Mechanics and Pysics of Soils, Vol.21

Mroz,Z., Norris,V.A. & Zienkiewicz,O.C.(1979), "Application of an anisotropic hardening model in the analysis of elasto-plastic deformation of soils", Geotechnique, Vol.29, No.1

Mroz,Z., Norris,V.A. & Zienkiewicz,O.C.(1981), "An anisotropic, critical state model for soils subjected to cyclic loading", Geotechnique, Vol.31, No.4

Norris,V.A.(1986), "Numerical modelling of soil response to cyclic loading using 'stress reversal surfaces'", Geomechanical modelling in engineering practice",edited by R.Dungar et al.

Shiomi,T. & Zienkiewicz,O.C.(1984), "Dynamic behaviour of saturated porous media; the generalised Biot formulation and its numerical solution", Takenaka Technical Report, No.31